

NNT : ***

n°LAL : ***

Thèse de doctorat

Search of the $0\nu\beta\beta$ decay with the SuperNEMO demonstrator

Thèse de doctorat de l'Université Paris-Saclay
préparée à l'Université Paris Saclay au sein du Laboratoire Irène-Joliot Curie
(anciennement Laboratoire de l'Accélérateur Linéaire)

École doctorale n°576 Particles, Hadrons, Energy, Nuclei, Instrumentation,
Imaging, Cosmos et Simulation (PHENIICS)
Spécialité de doctorat : Physique des particules

Thèse présentée et soutenue à Orsay, le ***, par

CLOÉ GIRARD-CARILLO

Composition du Jury :

***	Président

***	Rapporteur

***	Rapporteur
Christine Marquet CENBG - Bordeaux-Gradignan	Examineur

***	Examineur

***	Examineur
Laurent Simard LAL - Orsay	Directeur de thèse
Mathieu Bongrand LAL - Orsay	Co-directeur de thèse

Contents

Contents	3
Introduction	7
1 Phenomenology of particle physics	9
1.1 The Standard Model of particle physics	9
1.1.1 Bosons	9
1.1.2 Fermions	9
1.1.3 $2\nu\beta\beta$ decay	9
1.1.4 Where the Standard Model ends	9
1.2 Going beyond the Standard Model with neutrinos	9
1.2.1 Neutrino flavors and oscillations	9
1.2.2 Neutrino masses and nature	9
1.2.3 Other searches beyond the Standard Model with neutrinos . .	9
2 $0\nu\beta\beta$ experiment status	11
2.1 Experimental design criteria	11
2.1.1 Aspects of the nuclear matrix elements	12
2.1.2 Quenching	12
2.2 $0\nu\beta\beta$ direct search experiments	12
2.2.1 Semiconductors	12
2.2.2 Bolometers	13
2.2.3 Time projection chambers	14
2.2.4 Scintillators	16
2.2.5 Tracking calorimeters	16
3 The SuperNemo demonstrator	19
3.1 The SuperNemo demonstrator	19
3.1.1 Comparison with Nemo3 experiment	19
3.1.2 Experimental design	19
3.1.3 Sources	19
3.1.4 Tracker	19
3.1.5 Calorimeter	19

3.1.6	Calibration systems	19
3.1.7	Control Monitoring system	19
3.1.8	Electronics	19
3.2	The SuperNemo software	19
3.2.1	Simulation	19
3.2.2	Reconstruction	19
4	Analysis tools	21
4.0.1	Internal probability	21
4.1	Simulations	22
4.1.1	Modifications of simulation software	22
4.1.2	Internal background simulations	22
4.1.3	$0\nu\beta\beta$ simulations	22
5	Time difference	23
5.1	Principle and goal	23
5.1.1	Internal conversion	23
5.2	Analysis	24
5.2.1	Topological cuts	24
5.2.2	Exponentially modified Gaussian	24
5.2.3	Results	24
5.3	Conclusion	24
6	Detector commissioning	27
6.1	Reflectometry analysis	27
6.1.1	Goal of the reflectometry analysis	27
6.1.2	Pulse timing: controlling cable lengths	28
6.1.3	Signal attenuation	32
6.1.4	Pulse shape analysis	34
6.1.5	Comparison with ^{60}Co	35
6.2	Calibrating the electronic boards	35
6.2.1	Principle	35
6.2.2	Measuring the time offset of front end boards	35
6.2.3	Results	35
7	Characterisation of the calorimeter time resolution	37
7.1	Time calibration with a Cobalt source	37
7.1.1	Time response of optical modules	37
7.1.2	Experimental setup	41
7.1.3	Determination of the individual timing resolution of each optical module	41
7.2	The Light Injection System	41
7.2.1	Light injection system commissioning	42

<i>CONTENTS</i>	5
7.2.2 Time resolution of optical modules	42
Conclusion	43
Bibliography	45

Chapter 6

Detector commissioning

The commissioning of the SuperNEMO demonstrator has begun in 2019 and first calorimeter data was taken.

The calorimeter of SuperNEMO is segmented in 712 optical modules (OM), each composed by a coupling between a photomultiplier tube (PMT) and a polystyrene scintillator bloc (see Sec. 3.1.5 for more details). The divider of a PMT is connected to 2 cables, one providing the high voltage (HV), the other one, called signal cable, is a coaxial cable collecting and transporting the charge provided by the PMT.

By the summer 2020, the SuperNEMO demonstrator will be encapsulated in an anti radon tent. The so called *patch panel* will insure passage of cables from the inside, to the outside of the anti radon tent, therefore doubling the amount of cables needed for the calorimeter. We refer to the cables running from detector to patch panel as *internal* cables, and the cables from patch panel to the electronic boards as *external* cables. Consequently, regarding only the calorimeter part, 2848 cables were cut, assembled, connector-mounted, transported and installed at LSM. Then the check of every cable condition is mandatory to control and eventually fix them.

6.1 Reflectometry analysis

6.1.1 Goal of the reflectometry analysis

Taking into account the final demonstrator design, each coaxial length was determined, cables were cut and labelled in LAL, Orsay. All external coaxial cables were designed to be 7 meters-long – the distance between electronic boards and patch panel being the same for all channels at electronic boards – and internal cable lengths have been adapted to fit the distance from the patch panel to each optical module. Then, cutting and labelling all cables lasted several weeks. After all cables were transported and installed at LSM, we had to check each coaxial cable condition, for several reasons:

- check if no cable was damaged during the transport and the installation;

- control if no swap between cables has been made during cable labelling or calorimeter cabling,
- check if the coaxial cable was cut at the right length,
- more importantly estimate the signal time delay due to the cable lengths: knowing that the velocity of electrons in the coaxial cables has a known constant value, the longer is the cable, the more the signal takes time to travel from the PMT to the electronic channel. Therefore, each coaxial cable length has to be characterised, especially if we want to do time coincidences between two signals in two different channels.

To do so, a pulse, called *primary* pulse, is generated at the electronic board readout. The signal will travel all along the coaxial cable, from the electronic board to the PMT divider. Whether the cable is correctly connected to the PMT or not, the signal reflects at the other end. Then the signal travels back from the PMT to the

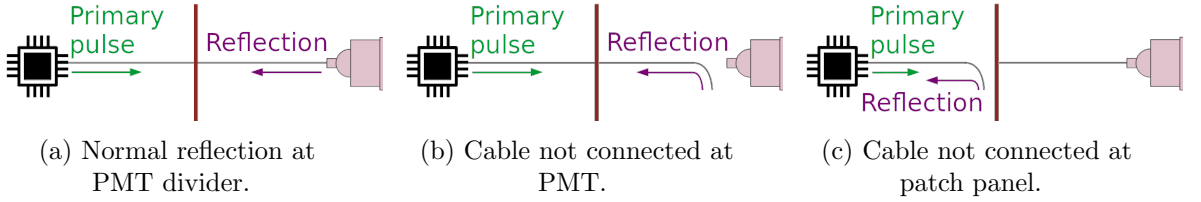


Figure 6.1: A representation of pulses sent in a cable for the reflectometry analysis is given. The electronic boards are symbolised by the black chip, and the patch panel by the red vertical bar. Three scenarios where a primary pulse is sent in one cable (represented in grey), are represented. (a) The cable is well connected at the patch panel and at the PMT. The signal reflects at the PMT divider. (b) The cable is not connected at PMT and the signal is reflected at the end of the cable. (c) The cable is not connected at patch panel and the signal is reflected at the end of the external cable.

electronic board channel, where it is recorded by the acquisition. We called this recorded reflected pulse *secondary* pulse. An example of the total recorded signal is displayed in Fig. 6.3a. In order to accumulate enough statistics, we send thousands of pulses in each coaxial cable. The analyses of the shape and of the arrival time of those secondary pulses for each channel is called *reflectometry*, and allow us to check the coaxial cable conditions and to control their lengths.

6.1.2 Pulse timing: controlling cable lengths

The first step of this analysis is to experimentally determine the length l_j^m for all signal cables j installed on the demonstrator. This length is defined as

$$l_j^m = 0.5 t_j v_p, \quad (6.1)$$

where t_j stands as the time made by the electrons to do a round trip between one electronic channel and one PMT, and v_p is the velocity of electrons in the coaxial cables, which can be expressed as a fraction of light speed in vacuum, c . The time difference t_j between the primary pulse and the secondary pulse is written as

$$t_j = \langle t_{\text{secondary pulse}} - t_{\text{primary pulse}} \rangle_p, \quad (6.2)$$

$\langle \rangle_p$ being the average over all pulses sent in one single cable j . The velocity v_p is supplied by the cable manufacturer as

$$v_p = \frac{c}{\sqrt{\epsilon_r}},$$

with ϵ_r the relative dielectric constant of the material. Therefore, this celerity depends on the components. For the coaxial cables chosen in the demonstrator design, the data sheet of the cable gives $v_p = 0.69c$. A study is performed to verify experimentally the value of v_p . Three cables of different lengths are measured with a precision of 1 cm. A thousand of primary pulses are sent in each of the three cables, then the time for each secondary pulse is recorded. At the end, we have three independent measures of the velocity v_p in the used coaxial cables. On Fig. 6.2 is displayed the lengths l_j as a function of the times t_j . The fitted value of $v_p/c = 0.697 \pm 0.0011$ is

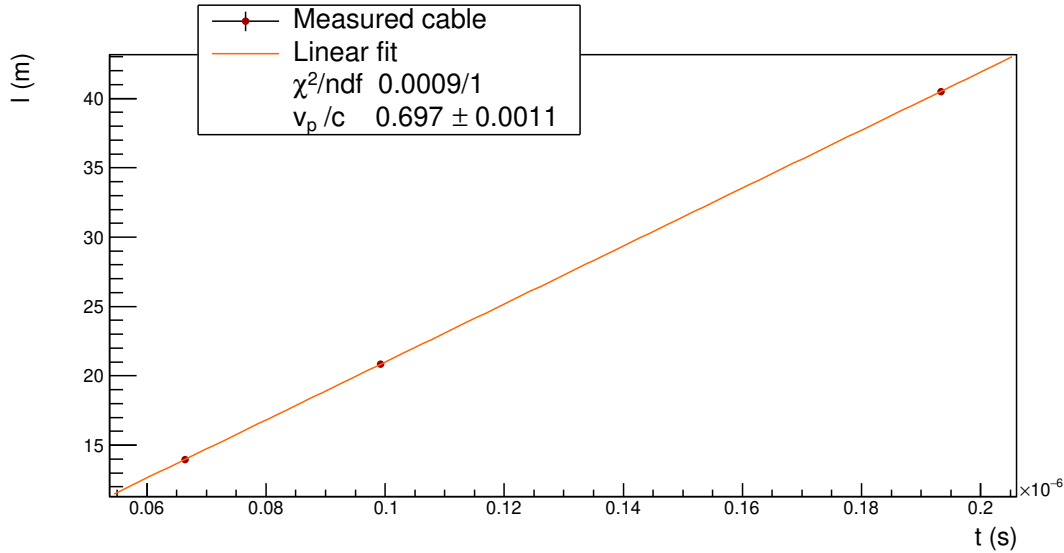


Figure 6.2: Three different lengths l_j of cables are measured. Pulses are sent inside all cables. The lengths l_j are plotted as a function of the time differences t_j between primary and secondary pulses. The value of v_p/c fitted from the data points is displayed. This value of 0.697 ± 0.0011 shows the compatibility with the one supplied by the constructor, of $0.69c$.

displayed and shows a compatibility up to 7σ with the data sheet.

As we want to determine the time interval t_j , we have to define what is the *time* of a pulse. In this analysis, we use a technique called Constant Fraction Discriminator (CFD), providing an amplitude-independent information about time of a pulse. This algorithm aims at tracking a signal and defining its time arrival at a given fraction f of its maximal amplitude. The two main advantages of this technique is that it provides an efficient rejection of the noise in the acquisition window, and gives a good resolution on the measured time. Nevertheless, the possible influence of the chosen value for the f parameter on this time resolution has to be investigated. We perform such a study in Sec. ???. We concluded that the highest precision on the time measurement arises for $f = 40\%$, and we adopt this value for the following analysis. A graphic representation of the CFD time search is given in fig. 6.3b. As we want to measure the installed cable lengths l_j^m , and compare them to the initially designed ones, l_j^d , we define the length difference ΔL_j as:

$$\Delta L_j = l_j^m - l_j^d. \quad (6.3)$$

On Fig. 6.4 is displayed the distribution ΔL for all the measured lengths. In hypothetical perfect conditions, all the cables should fit the design length, in other words, $l_j^d = l_j^m$. Consequently the ΔL distribution should a peak at zero, as materialised by the black dashed line. However, in real conditions, the measured length can be different from the designed one, leading the ΔL distribution plotted in orange solid line. We conclude that the observed cable length l^m differs from l^d by $+10.9 \pm 0.3$ cm, meaning that cables are longer than expected in average. This may reveal a bias coming from the device used to cut the cables. In fact, during cable cutting work, we noticed that the cutting device had a tendency to slip, probably leading to cables with extra lengths. We assumed the cutting device has a given probability to slip for one meter of cable. If this is the case, the probability for the device to give extra length should increase with the cable length.

To verify this assumption, we plot on Fig. 6.5 the length difference ΔL as a function of the initial design length l^d (cyan). From those data points, we compute a linear fit (orange solid line), parameterised as $y = \alpha x + \beta$, revealing that the cutting device presents two different biases. The value of β shows that the cutting device systematically took away 3.4 cm of each cable. Nevertheless, as the shortest cable was designed to be 10 meters long, there are no important consequences of this bias on the length difference ΔL . Besides, the slope $\alpha = 0.010 \pm 0.002$ of the linear fit reveals that the cutting device adds one centimetre for every meter of cable, being compatible with the hypothesis on the cutting device sliding. Hopefully this bias is not problematic as it makes most of the actual cable lengths longer than the design, while shorter lengths could have lead to systematic connection issues to PMTs. However, we notice that a few cables have been cut too short by mistake, the worse of them being 80 centimetres shorter than expected. Fortunately, this cable was successfully connected to PMT despite this deficit. On the contrary, few cables have a large extra length. This probably is due to human punctual mistakes on top of the observed bias, but without any strong consequences for the calorimeter operation.

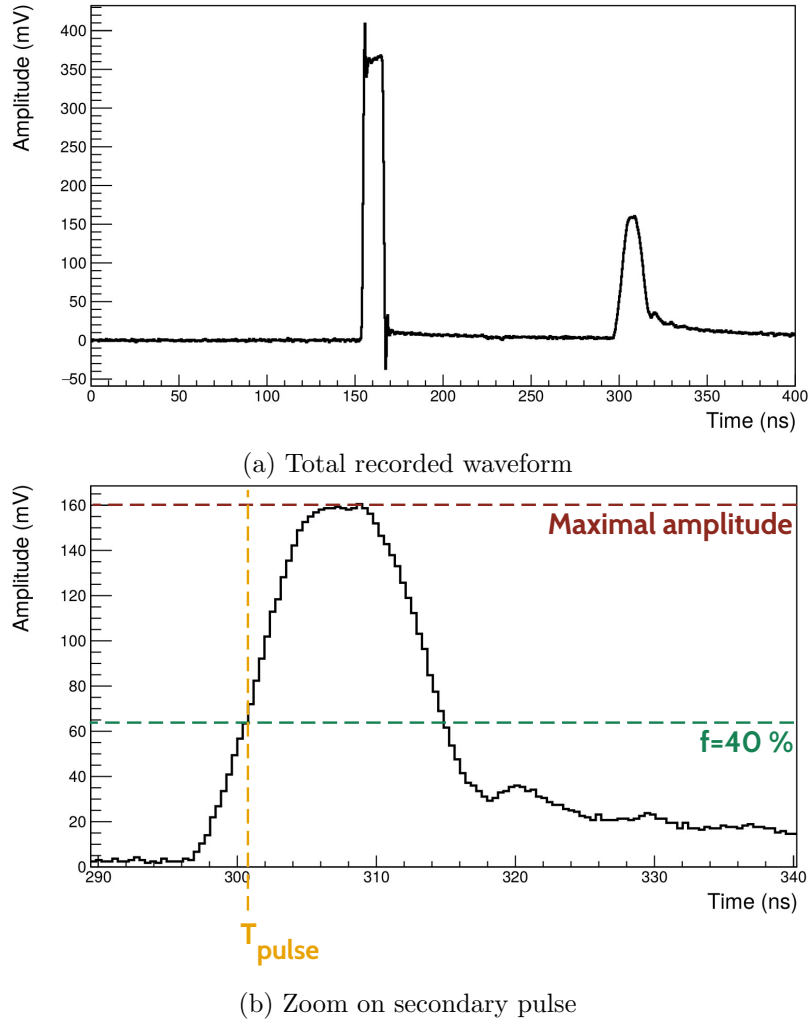


Figure 6.3: (a) Total recorded waveform: primary pulse (left) and secondary the pulse (right). (b) Zoom on the secondary pulse. A representation of time computed with a Constant Fraction Discriminator (CFD) is provided. Its maximal amplitude (red dotted line) and its fraction for $f = 40\%$ (green dotted line) are displayed. The time T_{pulse} (orange dotted line) represents the time of arrival of the secondary pulse computed with CFD, with the fraction $f = 40\%$.

In conclusion, no important mistakes have been made when cutting cables, and we had no issue for connecting the only problematic cable.

If the main goal of this study is to check the lengths of coaxial cables, it also aims at correcting the time of recorded events, from the time made by the signal to travel from a PMT to an electronic channel. taking into account the time for the signal to travel through cables. This become possible with the reflectometry study we performed. Knowing real lengths of cables and using the celerity of the signal, we deduce the time needed for the signal to travel from one given PMT divider to

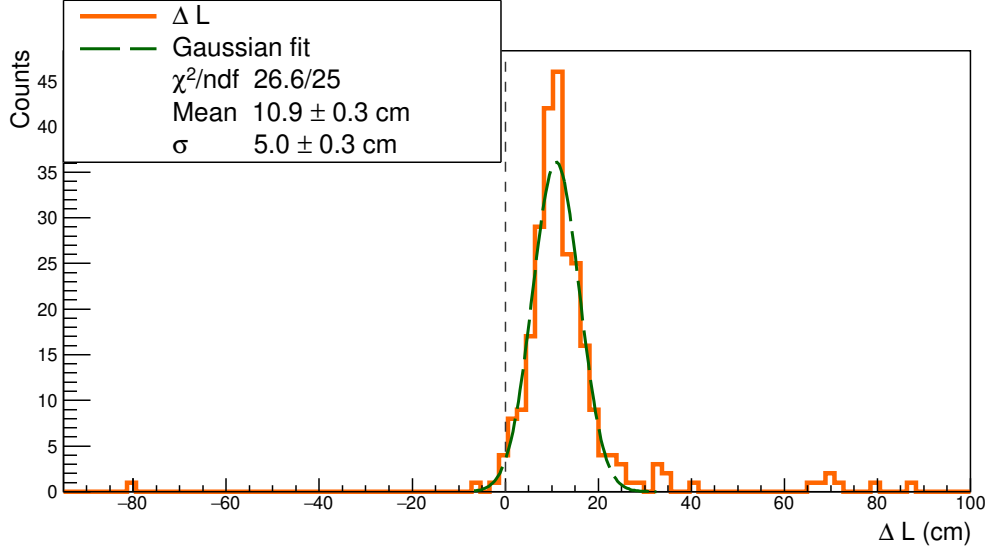


Figure 6.4: The distribution of difference between the measured lengths l^m and the expected lengths l^d is displayed in orange solid line. The black dashed line represents the case where $l_j^m = l_j^d \forall j$. The Gaussian fit (green dashed line) presents a mean of 10.9 ± 0.3 cm. Some data points considered as outliers are beyond 3σ .

the electronic boards. Then we can correct event times.

As explained previously, the time t_j gives information about the length of the cable j . We remind the coaxial cables are divided in two parts, one external and one internal, both linked by the so-called patch panel. Thus we can use that travel time to detect possible disconnection of a cable at patch panel. In fact, if one cable is not connected at the patch panel – this case is illustrated in Fig. 6.1c, – the pulse reflects at the end of the external cable part, going back to the electronic board. This very short time, giving information about the location of the reflection, is used to tag a patch-panel disconnection. Then, a simple check onsite can confirm this observation, and the external part of the cable can be connected to the patch panel.

This study allowed us to control and record the lengths of all coaxial cables installed on the SuperNEMO demonstrator at LSM, and gave information on the status of cable connections at patch panel. We also have understood the main results on measured cable lengths and the functioning and biases of the cutting device that we used.

6.1.3 Signal attenuation

The attenuation of an electric signal is a problem common to all electronic fields, and comes from the charge loss of an electromagnetic wave travelling in a medium. For a coaxial cable, this attenuation mainly depends on the signal frequency f in

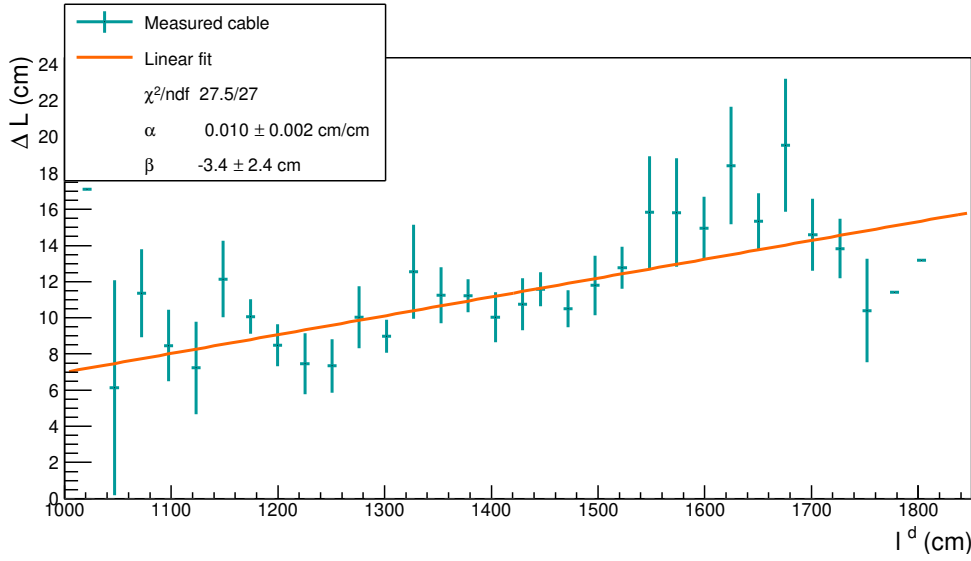


Figure 6.5: ΔL is plotted with l^d (cyan), where l^d is averaged for all the lengths designed to have the same value, being at the origin of vertical error bars. In black dashed line is represented the case where $l^m = l^m$. Data points are fitted by $\alpha x + \beta$, with $\alpha > 0$ and $\beta < 0$, revealing the two biases of the cutting device.

MHz and on the cable characteristics. For the coaxial cables, the theoretical linear attenuation $\alpha_{\text{att}}^{\text{th}}$, so be it the attenuation by metre of cable in dB/m, is supplied by the constructor as

$$\alpha_{\text{att}}^{\text{th}} = f\sqrt{\epsilon}\left(\frac{a}{\sqrt{f}} + b\right), \quad (6.4)$$

where the factor a depends on the diameter of the dielectric material on one side, and of the diameter of the conductor material on the other side, and where b is function of the dielectric loss factor, characterising the material's dissipation of electromagnetic energy. For the used coaxial cables, and with a frequency f of few GHz for the signal pulses sent in cables, we calculate this attenuation as $\alpha_{\text{att}}^{\text{th}} = 1.22$ dB/m. In a more general manner, the attenuation of a signal in dB is defined with the decimal logarithm of a power ratio. We use this definition to determine the attenuation in the framework of the reflectometry analysis, defining the attenuation \mathcal{A} , for a given length of cable l , as

$$\mathcal{A} = 10 \log_{10} \frac{V_{\text{primary pulse}}}{V_{\text{secondary pulse}}}, \quad (6.5)$$

where V_i is a quantity representing the intensity of the signal. V can correspond to the maximal amplitude of the pulse, as well as the *integrated charge* of the pulse, defined as the amount of current received by the acquisition over a given time window. As the provided data sheet does not specify the attenuation of which quantity (amplitude or charge) represents $\alpha_{\text{att}}^{\text{th}}$, we decide to investigate both in the following. Then, we

define the linear attenuation $\alpha_{\text{att}}^{\text{R}}$, measured by reflectometry in dB/m, with

$$\mathcal{A} = f_r + \alpha_{\text{att}}^{\text{R}} l, \quad (6.6)$$

with $f_r = -10 \log_{10} R$, where R is the reflection factor characterising the pulse reflection on the PMT divider. In fact, as the circuit is opened, the pulse is reflected at the PMT divider, but only partially. A part of the signal is not reflected but lost through the divider. This reflection is characterised by R , which is function of the impedance Z_c of the cable, and of the impedance Z_d at the divider level, where the pulse is reflected. It is written as

$$R = \frac{Z_d - Z_c}{Z_d + Z_c}, \quad (6.7)$$

where we have the limit

$$\lim_{Z_d \rightarrow \infty} f_r = 0 \text{ and } R = 1, \quad (6.8)$$

expressing a total reflection occurring when the impedance at the PMT divider is infinite. The main goal here is to determine the value of $\alpha_{\text{att}}^{\text{R}}$, using the reflectometry data, and to compare it with $\alpha_{\text{att}}^{\text{th}}$. Moreover, the impedance Z_d value at PMT divider can be estimated from the determination of f_r . On Fig. 6.6 is shown the linear dependence between the attenuation \mathcal{A} and the cable length l , and two data set are presented. The cyan scattered markers represent the attenuation calculated from the amplitude ratio $A_{\text{primary pulse}}/A_{\text{secondary pulse}}$, and the magenta markers correspond to the attenuation calculated from the charge ratio $Q_{\text{primary pulse}}/Q_{\text{secondary pulse}}$. The amplitude A_i is given in mV and the charge Q_i in mV.ns. The values of $\alpha_{\text{att}}^{\text{R}}$ and f_r , for both amplitude and charge cases, are displayed in the legend. Firstly, the two linear fits reveal that, whether calculated with the amplitude, or with the charge, the linear attenuation $\alpha_{\text{att}}^{\text{R}}$ is smaller than the calculated one $\alpha_{\text{att}}^{\text{th}}$ (for the amplitude case, $\alpha_{\text{att}}^{\text{th}} \simeq 5 \times \alpha_{\text{att}}^{\text{R, amp}}$, and for the charge case $\alpha_{\text{att}}^{\text{th}} \simeq 7 \times \alpha_{\text{att}}^{\text{R, ch}}$). That means the signal is less affected, when transmitted by the cable, than expected. Secondly, the attenuation in charge is less important than the attenuation in amplitude. This can be easily explained: as it is integrated over time, the charge is a quantity less affected by amplitude variations than the amplitude itself. For the same reason, the charge data set points are less spread than the amplitude ones, meaning that we are less sensitive to cable length variations when using the charge quantity.

This work achieved, we want to verify if no cable was damaged after installation. Reflectometry also aimed at checking cable conditions by performing waveform shape analysis on secondary pulses.

6.1.4 Pulse shape analysis

On Fig. 6.3 is displayed an example of *normal* pulse, which corresponds to the case represented in Fig. 6.1a. In this case, the pulse sent in the cable travels to the PMT, and goes back to the acquisition after reflection on the divider.

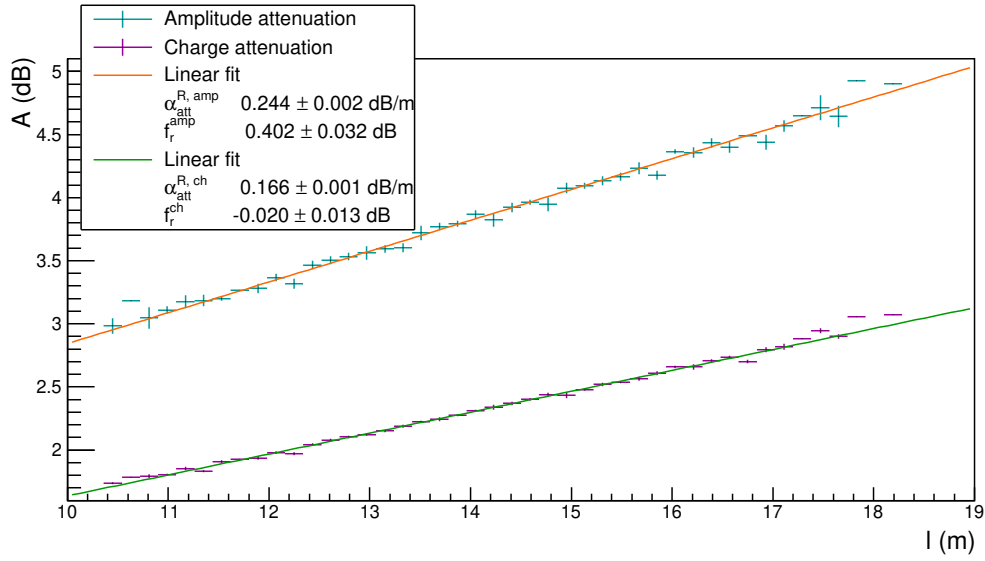


Figure 6.6: The amplitude \mathcal{A} is displayed as a function of the measured cable length l . The data set calculated with the amplitude (charge) is given in cyan (magenta) and fitted by a linear function in orange (green). The values of the slope, which represent the linear attenuation of the coaxial cables in dB/m, are respectively $\alpha_{\text{att}}^{\text{R, amp}} = 0.241 \pm 0.000 \text{ dB/m}$ and $\alpha_{\text{att}}^{\text{R, ch}} = 0.166 \pm 0.000 \text{ dB/m}$. The two y -intercept values, which represent the reflection of the pulse on the PMT divider, are $f_r^{\text{amp}} = 0.402 \pm 0.032 \text{ dB}$ and $f_r^{\text{ch}} = -0.020 \pm 0.013 \text{ dB}$.

6.1.5 Comparison with ^{60}Co

6.2 Calibrating the electronic boards

6.2.1 Principle

6.2.2 Measuring the time offset of front end boards

6.2.3 Results

Chapter 7

Characterisation of the calorimeter time resolution

The precise knowledge of the different particle interaction times in the optical modules of the SuperNEMO calorimeter is important to better understand and reject background. For example, the study of time-of-flight of electrons allows us to distinguish internal events (coming from source foils) from external events (PMTs, scintillators, tracker...).

In this chapter we present different studies conducted in order to characterise the time response of the SuperNEMO optical modules.

7.1 Time calibration with a Cobalt source

The Cobalt 60 disintegrates through β^- decays, to excited levels of Nickel 60. A simplified decay scheme for this atomic element is given in Fig. 7.1. The extreme majority of Cobalt β^- disintegration are followed by the emission of two γ 's of 1.17 MeV and 1.33 MeV. The life times of these two energy levels are very short, so the two photons are considered as emitted in coincidence with respect to the expected timing precision of the calorimeter. The goal of this analysis is to calibrate in time the SuperNEMO optical modules with a Cobalt 60 source, exploiting the time characteristic of those two emitted photons.

7.1.1 Time response of optical modules

A calorimeter block of SuperNEMO, composed of a scintillator and a photomultiplier, measures the scintillation light generated by the interaction of incoming particles. The energy of the incident particle, interacting electromagnetically (photon, electron, alpha...), is fully absorbed in the scintillator. The photons produced by the scintillating material are converted in electrons at the photomultiplier photocathode. After amplification, electrons are collected by the anode which delivers an electric

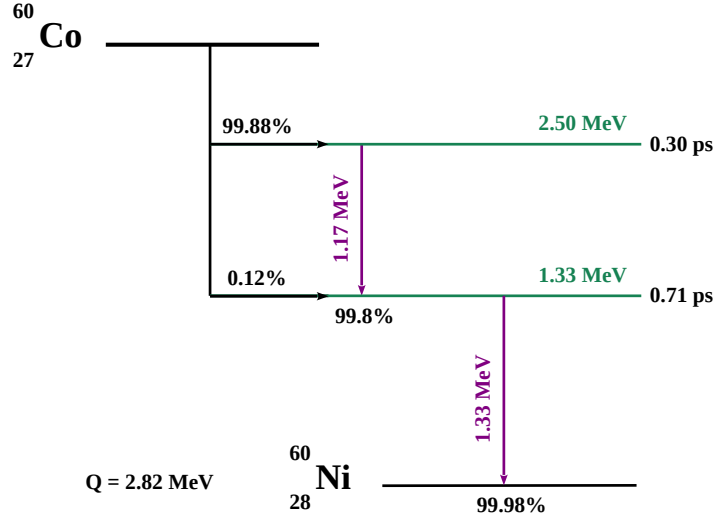


Figure 7.1: A simplified decay scheme for Cobalt 60. The Cobalt decays, through β^- , to one of the Nickel excited state. Then, two γ 's (whose energy levels are represented in green) are emitted in 99.66% of the cases. The two photons have an energy of 1.17 MeV and 1.33 MeV, respectively. As the life times of these two energy levels are short (< 1 ps), the two photons can be considered as emitted in coincidence. We use this property to calibrate in time the demonstrator optical modules.

signal whose charge is proportional to the initial amount of incident photoelectrons. This signal is then transmitted, via the PM voltage divider, to the electronic readout, where the signal is sampled. Energy and time of arrival of the incident particle can be extracted from the signal waveform analysis. Especially, the arrival time of the particle, defined in Fig 6.3b in Sec. 6.1, can be estimated. Each step, from the incident particle interaction inside the scintillator, to the signal sampling at the electronic readout, can have an impact on this arrival time measurement. On this section, we focus on the time resolution σ_t induced by the optical module, and written as

$$\sigma_t = \sqrt{\sigma_{t,\text{sc}}^2 + \sigma_{t,\text{PM}}^2}, \quad (7.1)$$

where the two terms $\sigma_{t,\text{sc}}$ and $\sigma_{t,\text{PM}}$ represent the time resolutions of the scintillator and of the PMT, respectively. We detail the physical origins of those terms.

Scintillator time dispersion

The temporal dispersion $\sigma_{t,\text{sc}}$ in Eq. (7.1) is based on the scintillator operating principle. When a particle interacts in the scintillator, two successive mechanisms of light absorption/re-emission take place. The excitation of scintillator molecules leads to the creation of fluorescence photons. Those photons are then absorbed and re-emitted by the POPOP agent at higher wavelengths. These two processes follow the same

temporal distribution

$$\mathcal{N}_{\text{photons}} = A \times e^{-t/\tau}, \quad (7.2)$$

with $\mathcal{N}_{\text{photons}}$ the number of generated photons at time t , A a normalisation constant and τ the fluorescence characteristic time of the considered process.

Another important phenomenon comes with the uncertainty on the interaction point location in the scintillator, which depends on the incident particle type. Depending on whether the incident particle is a photon or an electron, the term $\sigma_{t,sc}$ has a different contribution on the total time resolution σ_t . To picture this, we display the radiation length of photons and electrons in polystyrene on Fig 7.2. These figures

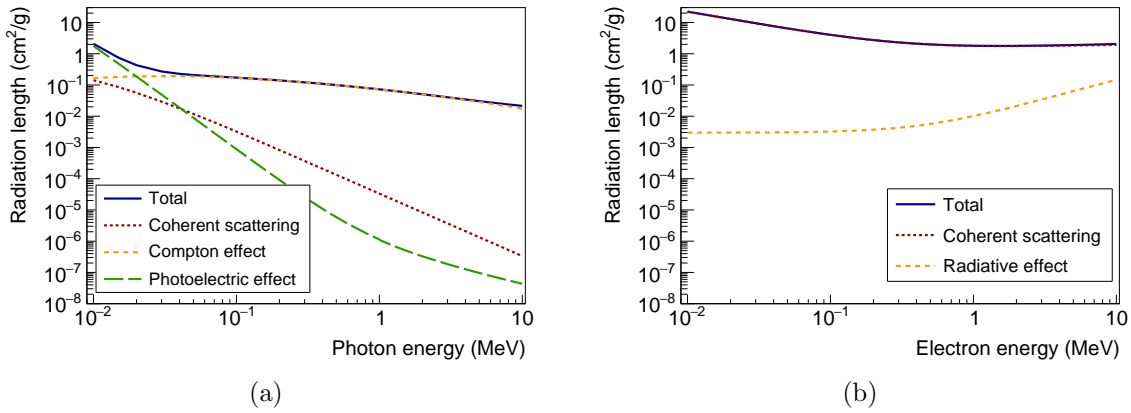


Figure 7.2: (a) Cross section of photons in polystyrene: coherent scattering (red dotted line), Compton effect (orange dotted line), photoelectric effect (green solid line) and total contribution (blue solid line). (b) Stopping power for electrons in polystyrene: coherent scattering (red dotted line), radiative effect (orange dotted line) and total contribution (blue solid line). At the considered energy range 10 keV – 10 MeV, the interaction of photons with matter is dominated by Compton effect, while the electrons interact mainly through coherent scattering. At same energies, a photon crosses roughly 10 times more polystyrene than an electron.

highlight that, at a given energy, a photon has roughly 10 times less probability to interact with polystyrene than an electron. Therefore, an electron has a high probability to be stopped in the first few millimetres of the scintillator, while a photon can interact in a large range of depth inside the detector volume.

On Fig 7.3 are schemed the interactions of a photon and that of an electron in a SuperNEMO scintillator. When the charged particle interacts in the scintillator, the absorbed energy leads to the emission of scintillation photons. They propagate inside the scintillator, in all directions from the interaction point, at the speed c/n_{sc} , with n_{sc} the optical index of the scintillator material. Depending on their initial direction, some of those photons propagate straightly to the PMT, and others are first reflected on the scintillator internal surface before entering the PMT, leading to time delay.

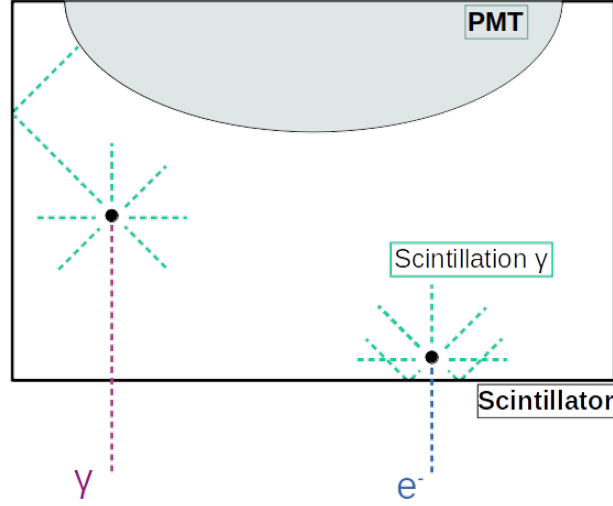


Figure 7.3: A scheme of interaction of particles in a scintillator. The photon case is displayed on the left in rose dotted line, and the electron case is on the right in dark blue dotted line. Both particles enter in the scintillator through the front face. Examples of interaction points inside the scintillator are represented by the black dots. The photons of scintillation emitted after the interaction are materialised by the bright green dotted lines. Due to different interaction probabilities in matter, the two particles are stopped at different depths inside the calorimeter. The photon can interact deeply inside the volume of the scintillating material while the electron has a high probability to interact within the first few millimetres.

To illustrate this phenomenon and give an order of magnitude of this effect, we take the example of an incident particle interacting in the middle of the scintillator. A photoelectron travelling straightly to the PM reaches the glass surface at $t_s = \frac{L}{2c/n_{sc}}$, L being the scintillator width, n_{sc} its optical index and c the speed of light. Now let us consider a photoelectron emitted in the opposite direction. It will propagate, reflect on the scintillator surface, and reach the PM at $t_r = \frac{3L}{2c/n_{sc}}$. This photon is then delayed of $\Delta t = t_r - t_s = \frac{L}{c/n_{sc}}$. Taking the width $L = 25$ cm and $n_{sc} = 1.5$, we obtain 1.25 ns of delay. Moreover, the more the incident particle interacts deeply inside the scintillator, the more those *reflected photons* are delayed. This mechanism increases the signal rising time collected at the PM anode, and impacts the scintillator time dispersion $\sigma_{t,sc}$. In addition, giving the cross sections of particles in polystyrene, this effect is more important for incoming photons than for incoming electrons. Therefore, we have $\sigma_{t,sc}^\gamma > \sigma_{t,sc}^{e^-}$.

Photomultiplier time dispersion

The second term $\sigma_{t,PM}$ in Eq. (7.1) describes the uncertainty on time measurement taken by the PMT. A photomultiplier is a photodetector whose time response de-

depends mainly on two parameters. Firstly, it depends on the transit time for the photoelectrons emitted at the photocathode to reach the anode after being multiplied. Secondly, the transit time of each photoelectron has a fluctuation, called transit time spread (TTS). Only this last parameter has an influence on the photomultiplier time dispersion $\sigma_{t,\text{PM}}$.

7.1.2 Experimental setup

7.1.3 Determination of the individual timing resolution of each optical module

Optical modules have been characterised before installation. Performing simulations of ^{60}Co disintegration

7.2 The Light Injection System

The SuperNEMO demonstrator is designed to have a long exposure time. In this context, calibration systems are necessary to control and calibrate the response of the detector. The so called *Light Injection* (LI) System will monitor the stability of the calorimeter response in energy to 1%. It consists in 20 Light Emitting Diodes (LED) at 385 nm, injecting light in each scintillator block via optical fibers. A set of reference optical modules (PMTs coupled with scintillator blocks), receiving light from both LEDs and ^{241}Am sources, monitors the stability of the LEDs. A scheme of the complete LI calibration system is given in Fig. 7.4.

First LI commissioning data was taken in March 2019.

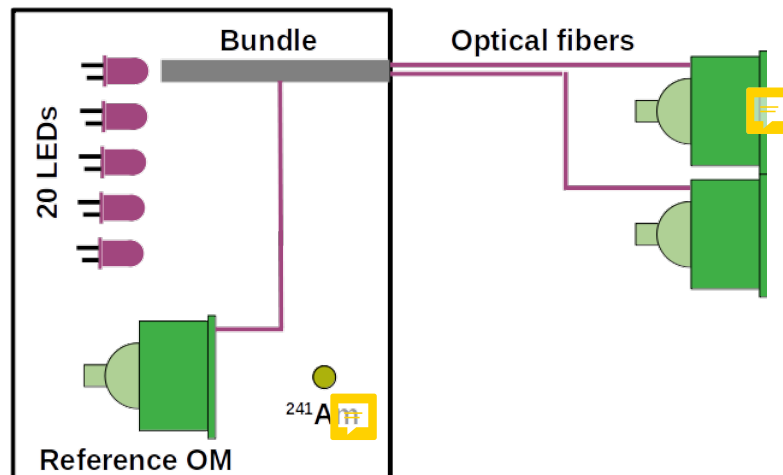


Figure 7.4: The Light Injection (LI) calibration system is schematised. More than 1300 fibers, distributed in 20 bundles, carry the light from 20 LEDs to each scintillator block of the demonstrator. Reference OMs coupled with ^{241}Am sources monitor the LED light.

7.2.1 Light injection system commissioning

In the LI system design, the SuperNEMO demonstrator has been segmented in 10 areas. Each area receives light from one given LED

Primary/secondary Each LED lights Group LEDs/area

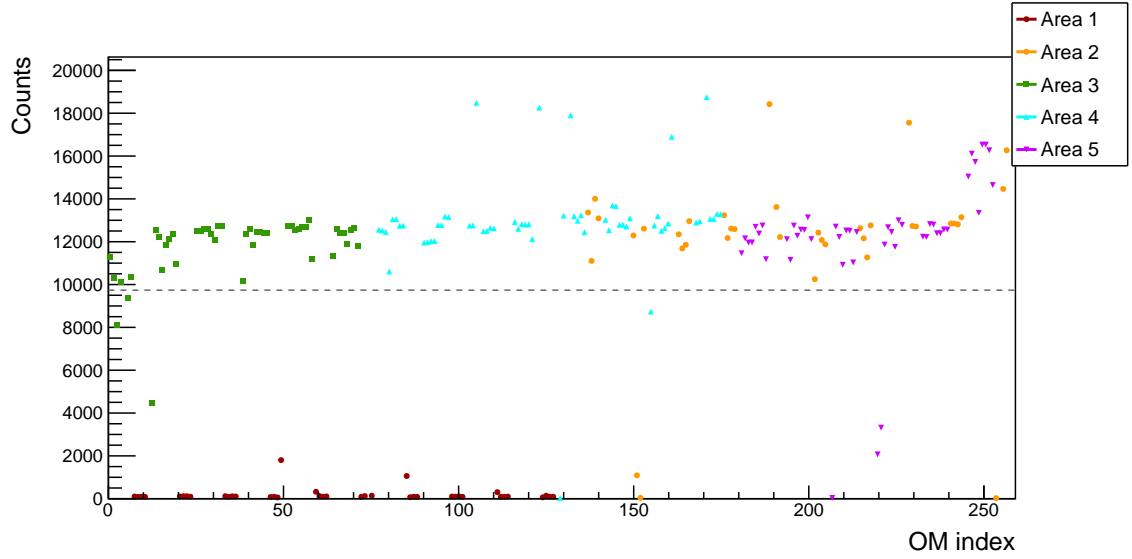


Figure 7.5: The number of counts is displayed for each optical module, labelled by the *OM index*. Each coloured marker represents counting rates for one area of the detector, that is to say one group of optical modules lighted by the same LED. The area #1 (dark red dots) is not receiving light from its corresponding LED.

7.2.2 Time resolution of optical modules

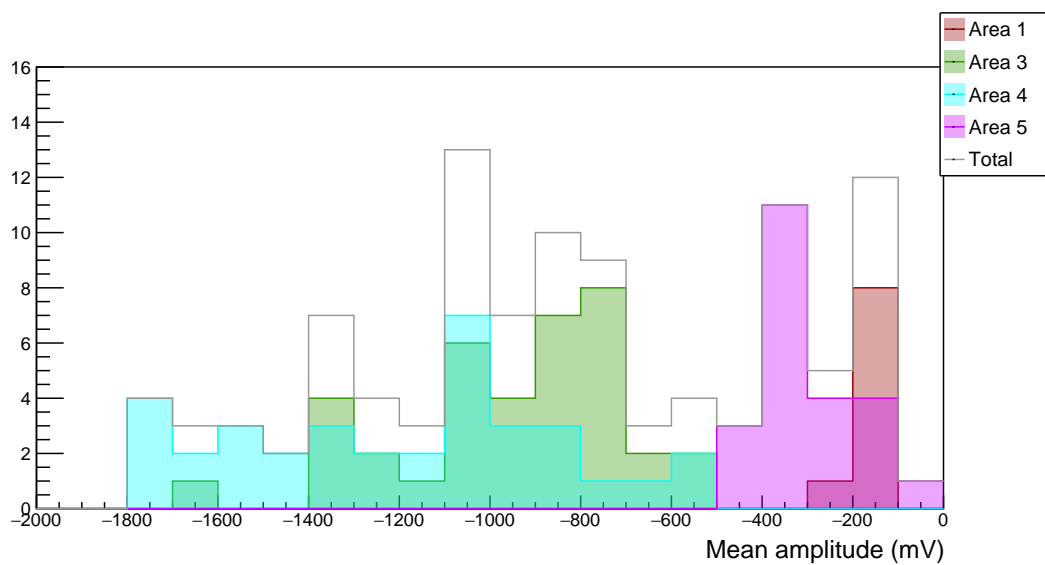


Figure 7.6: The mean signal amplitude distribution for each optical module is presented. One colour stands for one area of the half detector. In Grey is the total mean amplitude distribution.

Bibliography

- [1] M. et al. Agostini. Probing majorana neutrinos with double- β decay. *Science* 365, 1445, 2019.
- [2] S.I. et al. Alvis. Search for neutrinoless double-beta decay in ^{76}Ge with 26 kg-yr of exposure from the majorana demonstrator. *Phys. Rev. C*, 100, 2019.
- [3] O. et al. Azzolini. First result on the neutrinoless double- β decay of ^{82}Se with cupid-0. *Phys. Rev. Lett.*, 120:232502, Jun 2018.
- [4] C. et al. Alduino. First results from cuore: A search for lepton number violation via $0\nu\beta\beta$ decay of ^{130}Te . *Phys. Rev. Lett.*, 120:132501, Mar 2018.
- [5] J. B. et al. Albert. Search for neutrinoless double-beta decay with the upgraded exo-200 detector. *Phys. Rev. Lett.*, 120:072701, Feb 2018.
- [6] A. et al. Gando. Search for majorana neutrinos near the inverted mass hierarchy region with kamland-zen. *Phys. Rev. Lett.*, 117:082503, Aug 2016.